

Supplementary Information

Nuclearity Effect on Water Oxidation: A Comparative Study of Dinuclear and Mononuclear Iron Complexes

Rong Yan,^{abc} Zi-Han Li,^a Qian-Cheng Luo,^a Na-Na Sun,^{*a} Johnny C. Ho,^{*bc} and Yan-Zhen Zheng^{*a}

^a *Frontier Institute of Science and Technology, Interdisciplinary Research Center of Frontier Science and Technology, State Key Laboratory of Electrical Insulation and Power Equipment, MOE Key Laboratory for Nonequilibrium Synthesis and Modulation of Condensed Matter, Xi'an Key Laboratory of Electronic Devices and Material Chemistry, and School of Chemistry, Xi'an Jiaotong University, Xi'an, Shaanxi, 710054 P. R. China.*

^b *Department of Materials Science and Engineering, City University of Hong Kong, 83 Tat Chee Avenue, Kowloon 999077, Hong Kong.*

^c *Shenzhen Research Institute, City University of Hong Kong, Shenzhen 518057, P. R. China*

✉ Address correspondence: Sunnn@xjtu.edu.cn; johnnyho@cityu.edu.hk;
zheng.yanzhen@xjtu.edu.cn.

Chemicals and characterization

All chemicals were purchased from commercial sources and used without further purifications. X-ray crystallography data were recorded on a Bruker SMART CCD diffractometer with MoK α radiation ($\lambda = 0.71073 \text{ \AA}$). Powder X-ray diffraction data (PXRD) were collected using a Rigaku SmartLab diffractometer (Cu K α , $\lambda = 1.54184 \text{ \AA}$) at room temperature. High-resolution mass spectra (HR-MS) were recorded on a Q Exactive Plus mass spectrometer. Analytical gas chromatography (GC) for gas samples was carried out on a SHIMDZU GC-2014ATF/SPL (TDX-01 60/80 mesh, 2.0 mm \times 3.2 mm \times 2.1 mm FID, TCD-permanent gases, N₂ carrier gas). In-situ UV-vis absorption spectra were measured by a UV/Vis spectrometer (SR4, Ocean optics). Transmission spectra were collected using an FT-IR spectrophotometer (Nicolet iS50). Magnetic susceptibility measurements were performed on a powder sample fixed with Eicosane on a Quantum Design MPMS-XL7 SQUID magnetometer.

Synthesis of Fe(Pmabt)₂ (Fe-2S)

FeCl₂·4H₂O (0.08 g, 0.5 mmol), Fe(acac)₂ (0.10 g, 0.4 mmol), Et₃N (0.1 g), 2-pyridinecarboxaldehyde (0.1 g, 1 mmol), and 2-aminobenzenethiol (139 μ L, 1.3 mmol) were stirred in methanol (8 mL) for 15 min. The slurry was then sealed in a 12 mL glass vial and heated at 100°C for 24 h. Thereafter, the reactants were cooled to room temperature at a rate of 10°C/h. Dark-green rodlike crystals were collected, washed with methanol, and dried in nitrogen at room temperature (yield *ca.* 62% on the basis of Fe). Elemental analysis cal. (%) for C₂₄H₁₈FeN₄S₂: C 59.76, H 3.73, N 11.61; Found: C 59.74, H 3.74, N 11.60.

Synthesis of [Fe₂(Pmabt)₂(Pbt)₂][ClO₄]₂·2CH₃OH (2Fe-4S)

FeCl₂·4H₂O (0.10 g, 0.7 mmol), Fe(ClO₄)₂·6H₂O (0.08 g, 0.2 mmol), 2-pyridinecarboxaldehyde (0.1 g, 1 mmol), and 2-aminobenzenethiol (139 μ L, 1.3 mmol)

were stirred in methanol (8 mL) for 15 min. The slurry was then sealed in a 12 mL glass vial and heated at 100°C for 24 h. Thereafter, the reactants were cooled to room temperature at a rate of 10°C/h. Dark-violet block crystals were collected, washed with methanol, and dried in nitrogen at room temperature (yield *ca.* 34% on the basis of Fe). Elemental analysis cal. (%) for C₅₀H₃₈Cl₂Fe₂N₈O₁₁S₄: C 48.52, H 3.07, N 9.05; Found: C 48.49, H 3.09, N 9.04.

Electrochemical measurements

All experimental procedures were conducted under nitrogen at room temperature. The solution was bubbled with high-purity N₂ for at least 30 min before analysis. A standard three-electrode configuration was employed in conjunction with a CHI 660e. In all cases, a platinum auxiliary electrode and Ag/Ag⁺ reference electrode were used. Cyclic voltammetry (CV) was performed using a GC disk working electrode (diameter 3 mm, from CH Instruments Ins). CV curves were acquired in a mixed solvent (acetonitrile/H₂O = 8:2 v/v for **Fe-2S**, 9:1 v/v for **2Fe-4S**) containing 0.2 mM complex and 0.1 M Bu₄NPF₆. The working electrode was treated between scans by means of polishing with α -Al₂O₃ of decreasing sizes (1.0 μ m-50 nm) alumina paste (from BAS Inc.) and washing with purified H₂O and ethanol. Ferrocene was used as an internal standard, and all potentials reported within this work are referenced to the ferrocenium/ferrocene couple at 0 V. Controlled potential electrolysis (CPE) was performed in a custom-designed gas-tight cell using an indium tin oxide (ITO)-coated glass electrode (0.7 mm thick, 10 Ω /sq from Furuuchi Chemical Co. Ltd.). The ITO electrode was washed by ultrasonication in a methanolic solution of 0.5 M K₂CO₃ for 30 min and then rinsed with acetonitrile and purified water prior to use.

X-ray crystallographic analysis for Fe-2S and 2Fe-4S

Single-crystal X-ray diffraction data of **Fe(Pmabt)₂** (Fe-2S) and **[Fe₂(Pmabt)₂(Pbt)₂][ClO₄]₂·2CH₃OH** (2Fe-4S) were recorded on a Bruker Apex Duo diffractometer with Mo K α radiation ($\lambda = 0.71073$ Å) at 150 K. The structures were solved by direct methods and all non-H atoms were subjected to anisotropic refinement by full-matrix least-squares refinement on F^2 using Olex2 program. CCDC 2383667 (**Fe-2S**) and 2383668 (**2Fe-4S**) contain the supplementary crystallographic data for this paper. The data can be obtained free of charge via www.ccdc.cam.ac.uk/conts/retrieving.html (or from the Cambridge Crystallographic Data Centre, 12 Union Road, Cambridge CB21EZ, UK; fax: (+44)1223-336-033; or deposit@ccdc.cam.ac.uk).

Table S1: X-ray crystallographic data for complex **Fe-2S**.

Complex	Fe(Pmabt) ₂
Empirical formula	C ₂₄ H ₁₈ FeN ₄ S ₂
Formula weight	482.39
Crystal system	Orthorhombic
Space group	<i>Pna</i> 2 ₁
<i>a</i> / Å	23.582(8)
<i>b</i> / Å	7.927(3)
<i>c</i> / Å	11.326(4)
α / °	90
β / °	90
γ / °	90
<i>V</i> / Å ³	2117.3(13)
<i>Z</i>	4
ρ_{calc} / g cm ⁻³	1.513
<i>F</i> (000)	992.0
Radiation	Mo K α ($\lambda = 0.71073$)
2 θ range / °	3.454 to 51.048
Goodness-of-fit on F^2	1.042
Final <i>R</i> indexes [$I \geq 2\sigma(I)$]	$R_1 = 0.0206$, $wR_2 = 0.0506$
Final <i>R</i> indexes [all data]	$R_1 = 0.0219$, $wR_2 = 0.0512$

$$R_1 = \frac{\sum |F_o| - |F_c|}{\sum |F_o|}, wR_2 = \left\{ \frac{\sum [w(F_o^2 - F_c^2)^2]}{\sum [w(F_o^2)^2]} \right\}^{1/2}$$

Table S2: X-ray crystallographic data for complex **2Fe-4S**.

Complex	[Fe ₂ (Pmabt) ₂ (Pbt) ₂][ClO ₄] ₂ ·2CH ₃ OH
Empirical formula	C ₅₀ H ₃₈ Cl ₂ Fe ₂ N ₈ O ₁₁ S ₄
Formula weight	1237.72
Crystal system	Triclinic
Space group	<i>P</i> $\bar{1}$
<i>a</i> / Å	9.0102(7)
<i>b</i> / Å	11.9133(9)
<i>c</i> / Å	25.039(2)
α / °	84.209(3)
β / °	86.646(3)
γ / °	85.619(3)
<i>V</i> / Å ³	2662.7(4)
<i>Z</i>	2
ρ_{calc} / g cm ⁻³	1.544
<i>F</i> (000)	1264.0
Radiation	Mo K α (λ = 0.71073)
2 θ range / °	4.518 to 52.724
Goodness-of-fit on <i>F</i> ²	1.022
Final <i>R</i> indexes [<i>I</i> >= 2 σ (<i>I</i>)]	<i>R</i> ₁ = 0.0598, <i>wR</i> ₂ = 0.1547
Final <i>R</i> indexes [all data]	<i>R</i> ₁ = 0.0651, <i>wR</i> ₂ = 0.1594

$$R_1 = \frac{\sum ||F_0| - |F_c||}{\sum |F_0|}, wR_2 = \left\{ \frac{\sum [w(F_0^2 - F_c^2)^2]}{\sum [w(F_0^2)^2]} \right\}^{1/2}$$

Table S3: Selected bond lengths (Å) in complex **Fe-2S**.

Bonds	Lengths (Å)	Bonds	Lengths (Å)
Fe(1)-S(1)	2.2921(9)	Fe(1)-S(2)	2.3017(10)
Fe(1)-N(1)	1.916(2)	Fe(1)-N(2)	1.975(2)
Fe(1)-N(3)	1.914(2)	Fe(1)-N(4)	1.959(2)

Table S4: Selected angles (°) in complex **Fe-2S**.

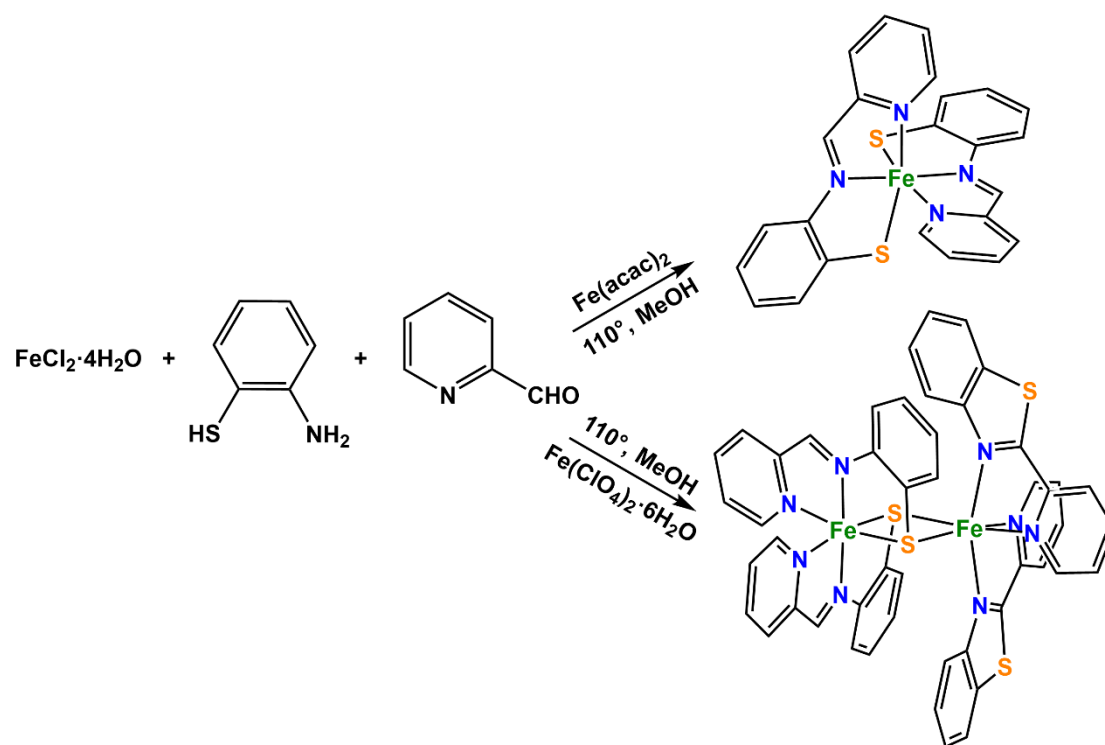
Bond angles	(°)	Bond angles	(°)
S(1)-Fe(1)-S(2)	91.13(3)	N(3)-Fe(1)-S(2)	86.03(8)
N(3)-Fe(1)-S(1)	96.18(7)	N(3)-Fe(1)-N(4)	81.51(11)
N(3)-Fe(1)-N(2)	96.42(10)	N(4)-Fe(1)-S(1)	86.81(7)
N(4)-Fe(1)-N(2)	96.00(9)	N(1)-Fe(1)-S(2)	98.28(7)
N(1)-Fe(1)-S(1)	85.87(7)	N(1)-Fe(1)-N(4)	94.30(10)
N(1)-Fe(1)-N(2)	81.64(9)	N(2)-Fe(1)-S(2)	88.79(7)
N(3)-Fe(1)-N(1)	175.21(10)	N(2)-Fe(1)-S(1)	167.36(7)

Table S5: Selected bond lengths (Å) in complex **2Fe-4S**.

Bonds	Lengths (Å)	Bonds	Lengths (Å)
Fe(1)-S(1)	2.3021(9)	Fe(1)-S(2)	2.2957(8)
Fe(2)-S(1)	2.5118(9)	Fe(2)-S(2)	2.4784(9)
Fe(1)-N(1)	1.914(3)	Fe(1)-N(2)	1.960(3)
Fe(1)-N(3)	1.952(3)	Fe(1)-N(4)	1.921(3)
Fe(2)-N(5)	2.221(3)	Fe(2)-N(6)	2.182(3)
Fe(2)-N(7)	2.192(3)	Fe(2)-N(8)	2.217(3)

Table S6: Selected angles (°) in complex **2Fe-4S**.

Bond angles	(°)	Bond angles	(°)
S(1)-Fe(1)-S(2)	91.10(3)	N(4)-Fe(1)-S(2)	85.90(8)
N(4)-Fe(1)-S(1)	97.02(8)	N(4)-Fe(1)-N(3)	81.84(11)
N(4)-Fe(1)-N(2)	95.52(11)	N(3)-Fe(1)-S(2)	167.70(9)
N(3)-Fe(1)-S(1)	89.34(8)	N(3)-Fe(1)-N(2)	93.08(11)
N(1)-Fe(1)-S(2)	95.77(8)	N(1)-Fe(1)-S(1)	85.75(9)
N(1)-Fe(1)-N(4)	176.74(11)	N(1)-Fe(1)-N(3)	96.52(12)
N(1)-Fe(1)-N(2)	81.72(12)	N(2)-Fe(1)-S(2)	89.14(8)
N(2)-Fe(1)-S(1)	167.44(9)	S(1)-Fe(2)-S(2)	82.25(3)
N(8)-Fe(2)-S(2)	97.88(8)	N(8)-Fe(2)-S(1)	97.43(8)
N(8)-Fe(2)-N(5)	161.26(11)	N(6)-Fe(2)-S(2)	169.25(8)
N(6)-Fe(2)-S(1)	90.89(8)	N(6)-Fe(2)-N(8)	91.19(11)
N(6)-Fe(2)-N(5)	76.15(12)	N(6)-Fe(2)-N(7)	92.58(10)
N(5)-Fe(2)-S(2)	96.33(8)	N(5)-Fe(2)-S(1)	96.55(8)
N(7)-Fe(2)-S(2)	95.16(8)	N(7)-Fe(2)-S(1)	172.85(8)
N(7)-Fe(2)-N(8)	76.26(11)	N(7)-Fe(2)-N(5)	90.35(11)
Fe(1)-S(1)-Fe(2)	92.80(3)	Fe(1)-S(2)-Fe(2)	93.84(3)



Scheme S1 Synthesis routine of two complexes.

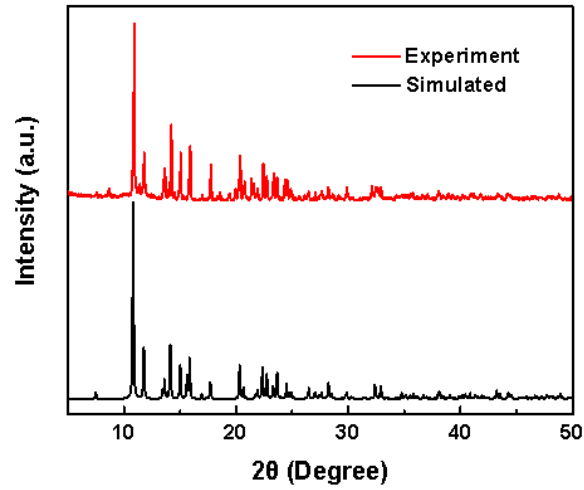


Figure S1 PXRD spectra and simulated pattern for Fe-2S.

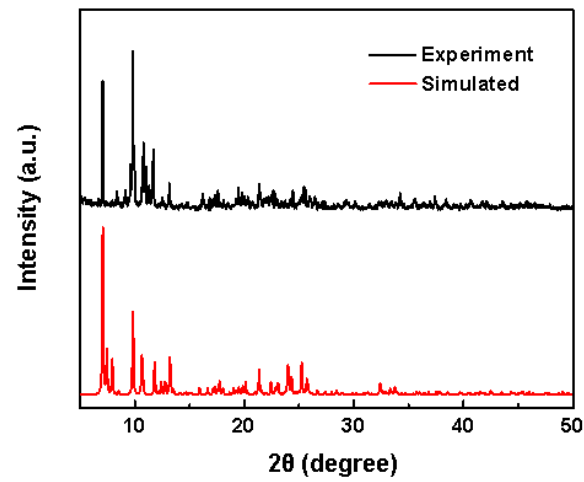


Figure S2 PXRD spectra and simulated pattern for 2Fe-4S.

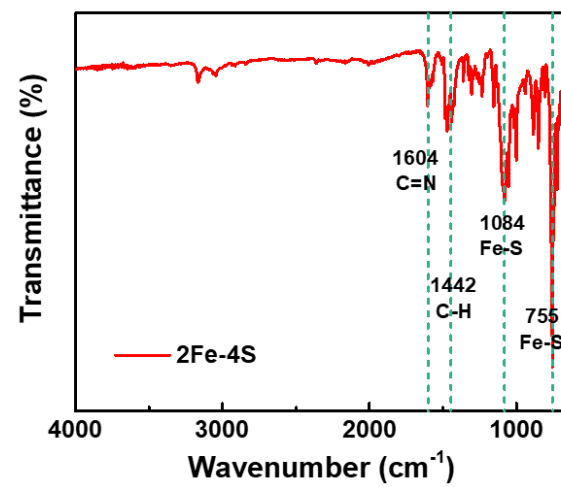


Figure S3 Infrared spectra of 2Fe-4S.

Magnetic Properties

Upon cooling, the $\chi_M T$ - T plot initially goes down smoothly and then drops abruptly below 25 K, finally falling to the minimum of $1.84 \text{ cm}^3 \text{ mol}^{-1} \text{ K}$ at 2 K. The sudden decrease at low temperature can be ascribed to the zero-field splitting (ZFS) of the high-spin Fe(II) ion. Then the M - H plot was recorded from 0-7 T at 2 K. The magnetization increases continuously with the increment of external magnetic field, and arrives at the maximum value of $3.40 \mu_B$ at 7 T, which is not saturated and corresponds to the computed value of $4 \mu_B$ for one free high-spin Fe(II) ion. To understand such magnetic behavior, we fitted the dc magnetic data through PHI program using the spin Hamiltonian for merely describing one high-spin Fe(II) center (equation 1).¹ Moreover, the TIP term was also considered, making the final magnetic susceptibility expressed by equation 2. The best fit gives TIP = $7.50 \times 10^{-3} \text{ cm}^3 \text{ mol}^{-1}$, isotropic Landé factor $g = 2.13$, and the axial and rhombic ZFS parameters of $|D|$ and $|E|$ are 11.28 and 3.75 cm^{-1} . Particularly, dc magnetic data can be reproduced by both positive and negative D and E values, indicating strong rhombicity of **2Fe-4S**.

$$\hat{H} = D \left(\hat{S}_z^2 - \frac{1}{3} \hat{S}(\hat{S} + 1) \right) + E \left(\hat{S}_x^2 - \hat{S}_y^2 \right) + \mu_B g \hat{S} \cdot \vec{B} \quad (1)$$

$$\chi = \chi_{\text{cal}} + \text{TIP} \quad (2)$$

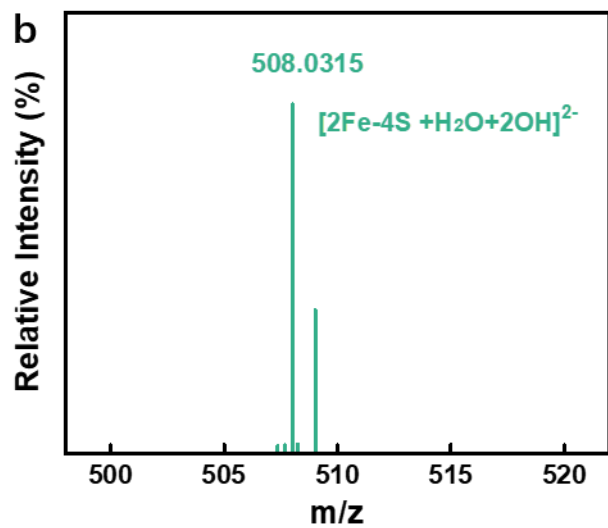
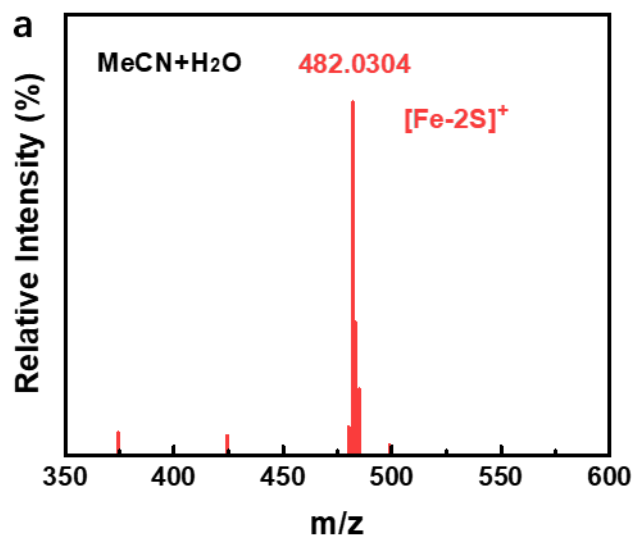


Figure S4 HR-MS in MeCN/H₂O solutions of (a) [Fe-2S]⁺ and (b) [2Fe-4S + H₂O + 2OH]²⁻.

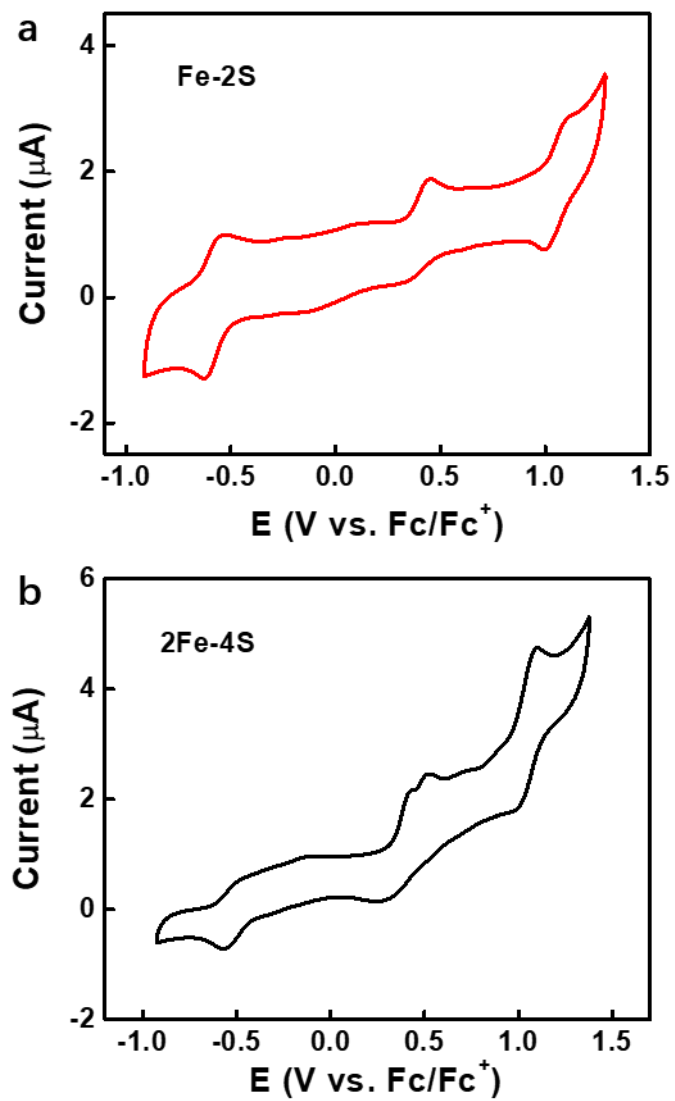


Figure S5 CV of (a) Fe-2S and (b) 2Fe-4S in MeCN with 0.1 M Bu_4NPF_6 at scan rate of 10 mV/s.

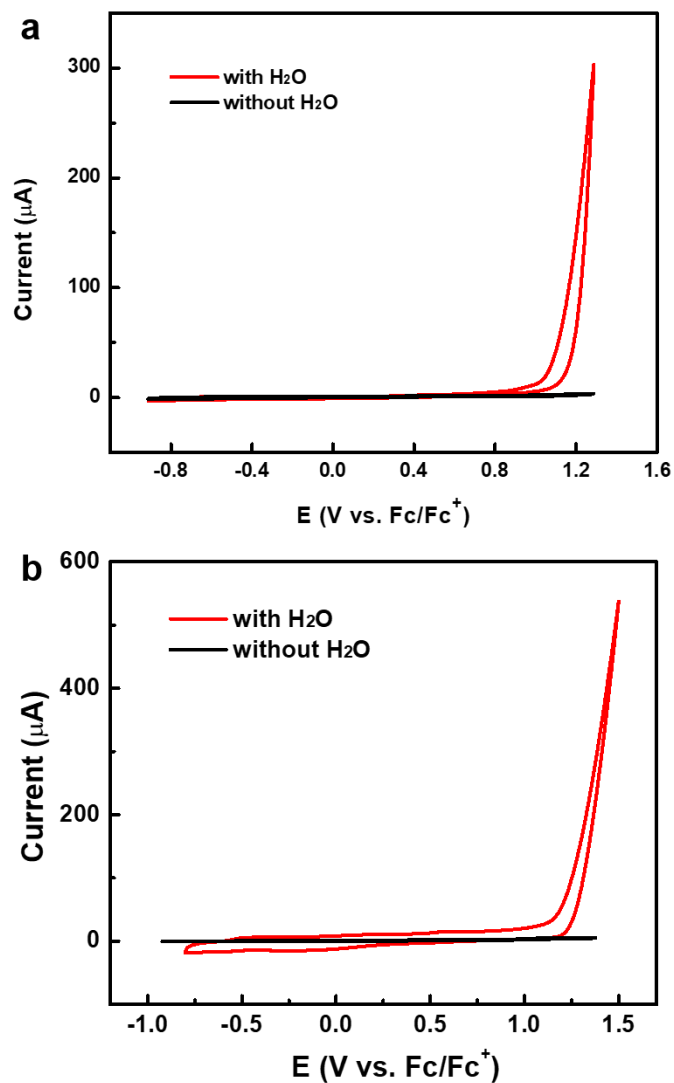


Figure S6 CVs of (a) Fe-2S with 10.1 mM H_2O (red line) and (b) 2Fe-4S in MeCN with 5.6 mM of H_2O (red line) and without H_2O (black line).

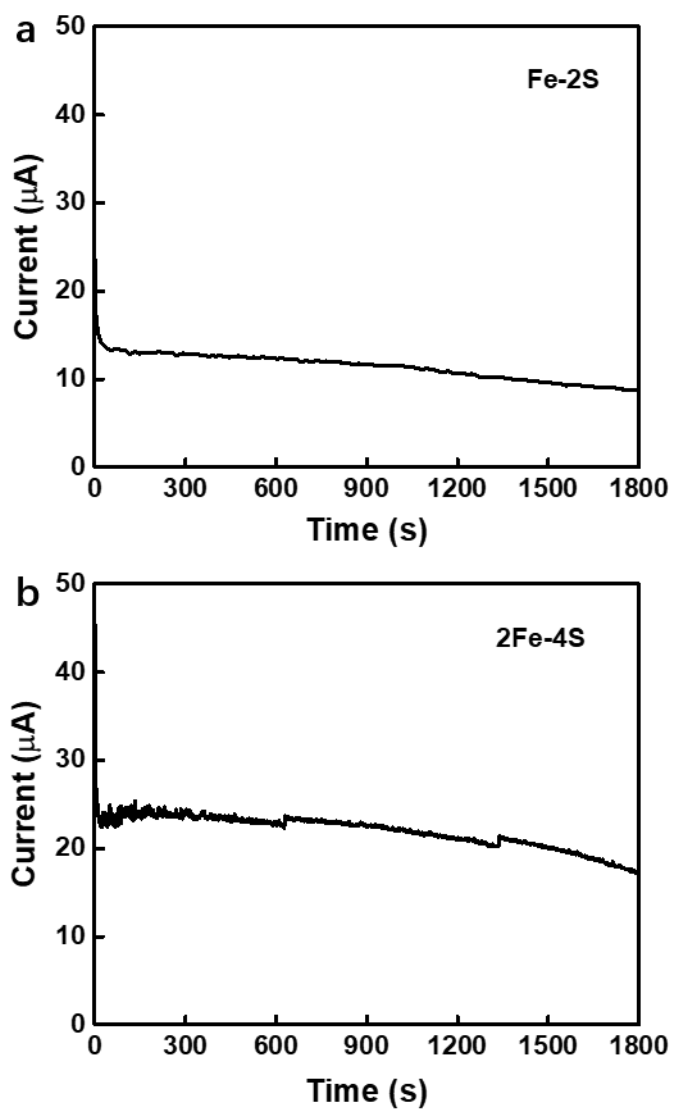


Figure S7 I-t curve of (a) Fe-2S and (b) 2Fe-4S corresponding to Q-t curves for CPE.

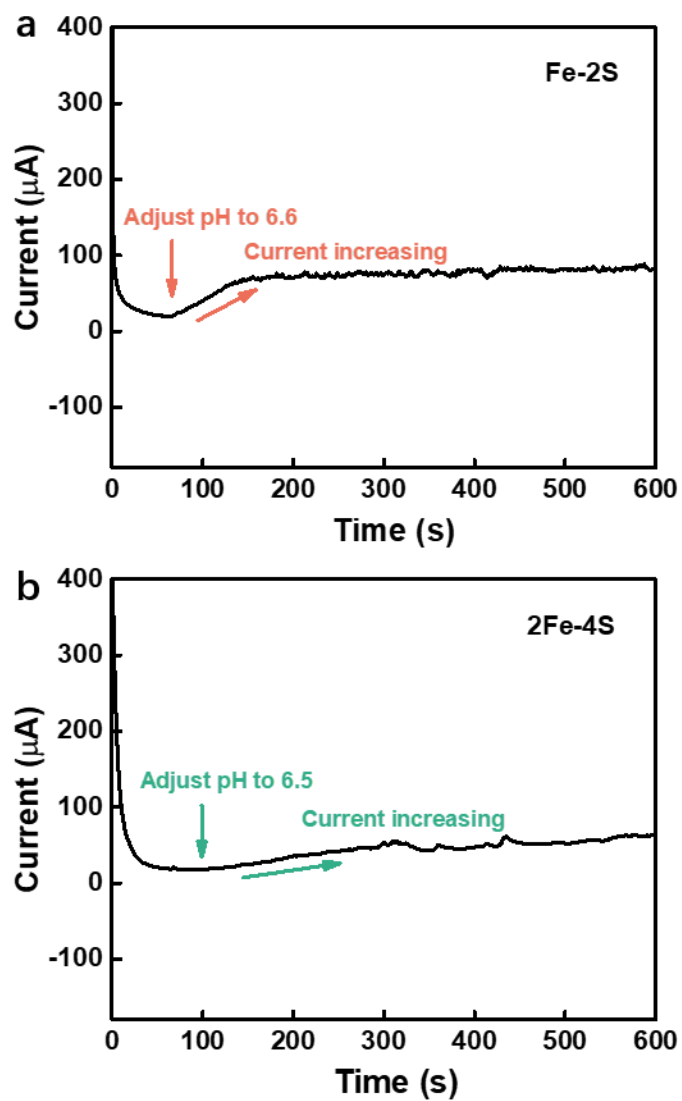


Figure S8 I-t curve of adjusting pH back to CPE experiment initial state for (a) Fe-2S and (b) 2Fe-4S.

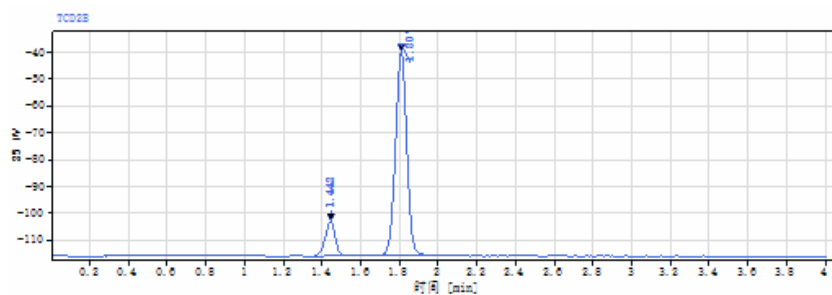


Figure S9 Oxygen evolution recorded by GC-MS of Fe-2S.

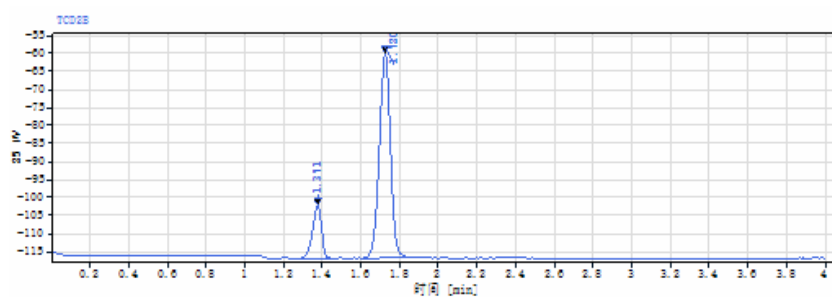


Figure S10 Oxygen evolution recorded by GC-MS of 2Fe-4S.

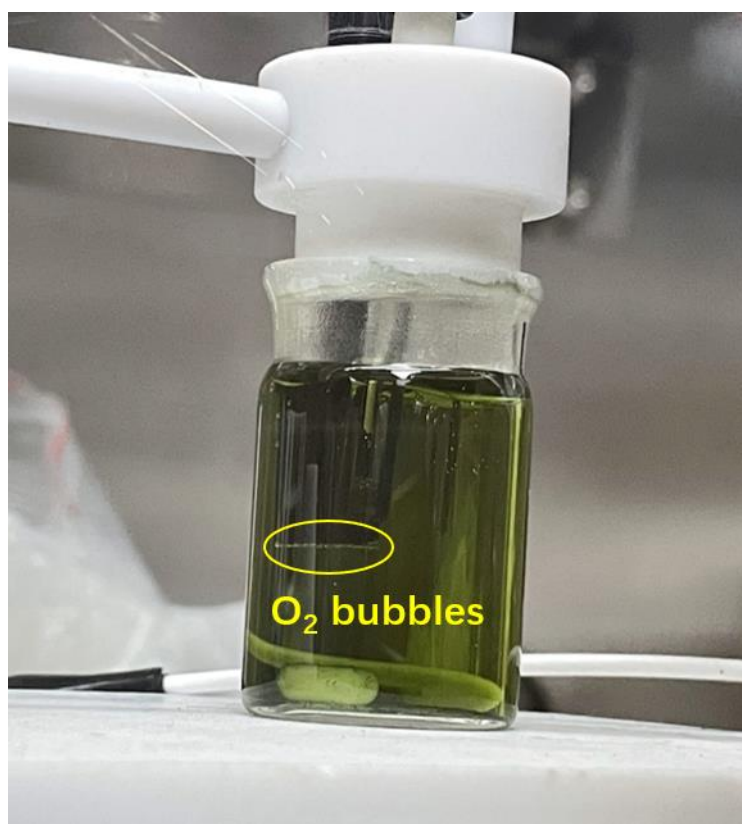


Figure S11 Oxygen bubbles generated on working electrode during CPE.

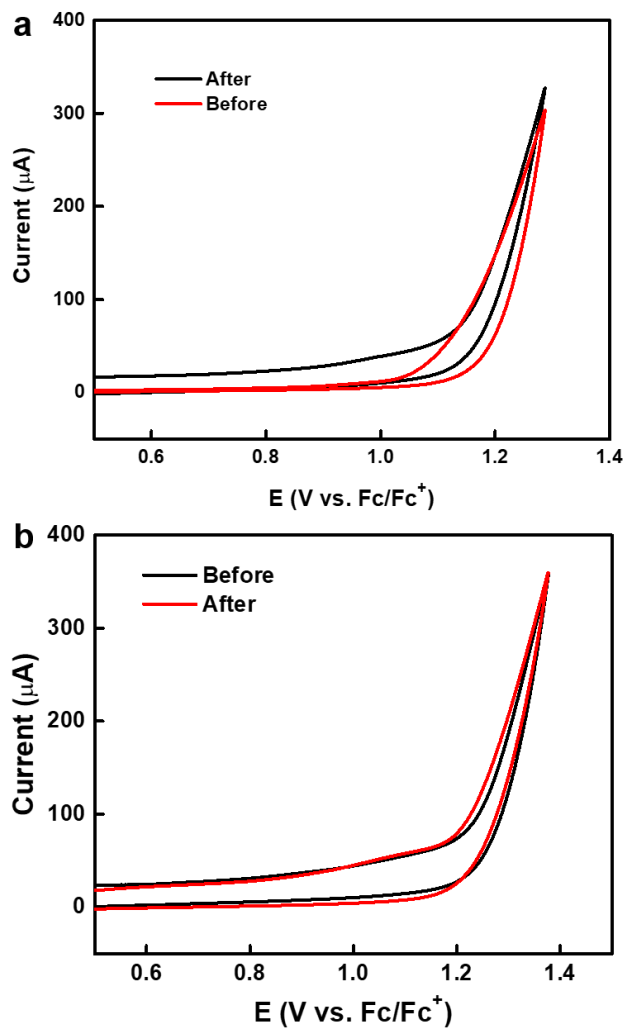


Figure S12 CVs of (a) Fe-2S before (red line) and after (black line) 30 minutes of electrolysis. (b) 2Fe-4S before (black line) and after (red line) 30 minutes of electrolysis in MeCN/H₂O with Bu₄NPF₆ (0.1 M).

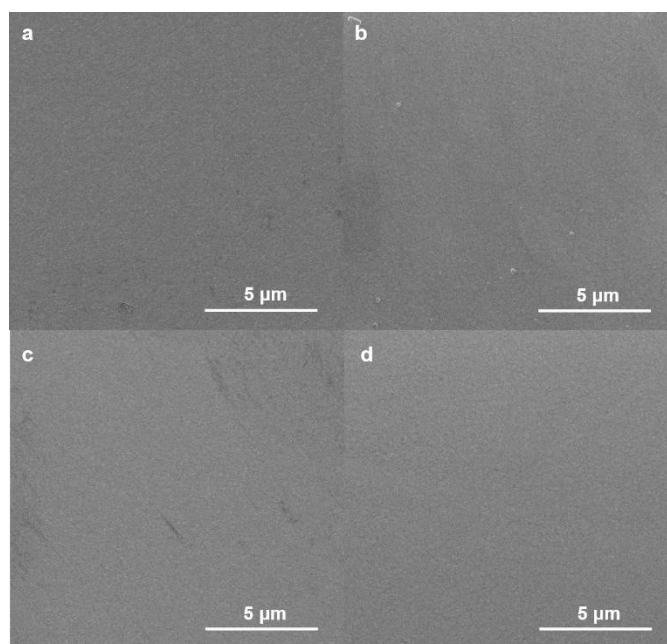


Figure S13 SEM images of ITO electrodes for **Fe-2S** (a) before and (b) after electrolysis. SEM images of ITO electrodes for **2Fe-4S** (c) before and (d) after electrolysis. The scale bars are 5 μm .

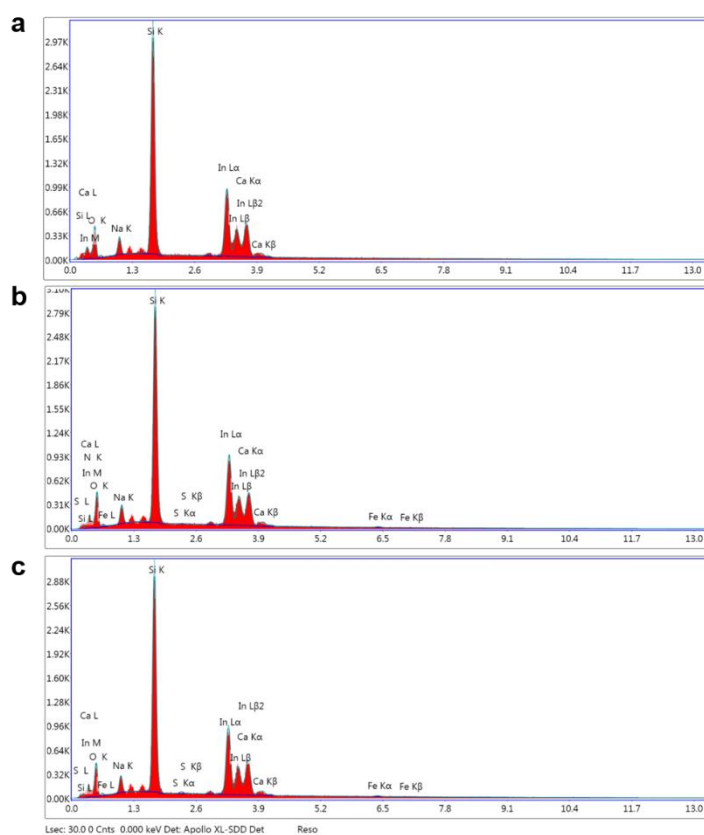


Figure S14 EDX mappings of ITO electrodes (a) before and after electrolysis for (b) **Fe-2S** and (c) **2Fe-4S**, respectively.

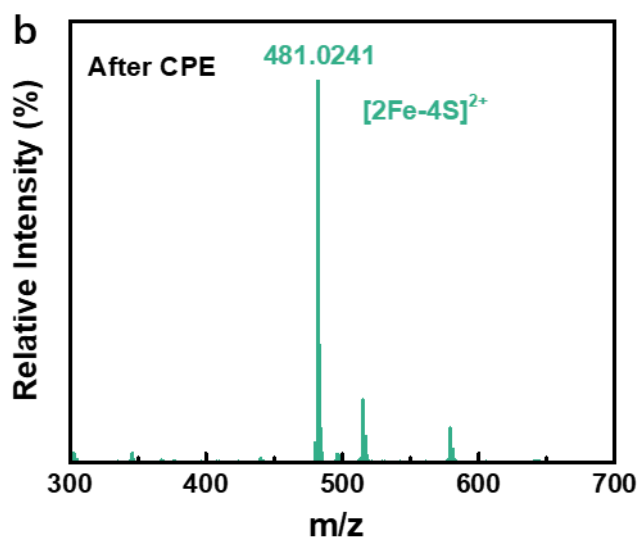
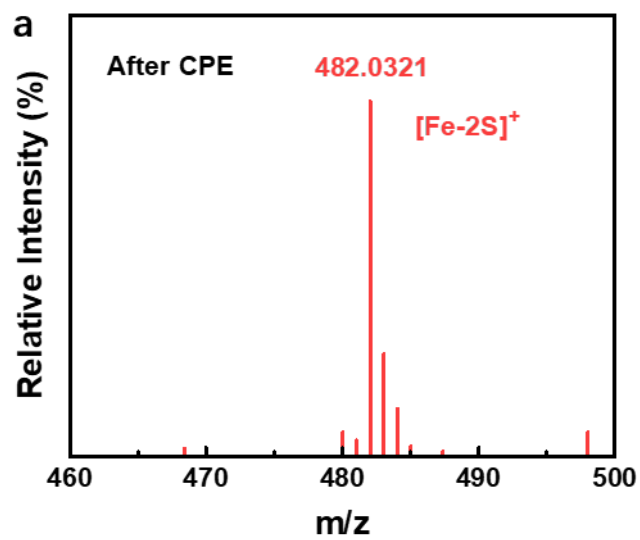


Figure S15 HR-MS of (a) [Fe-2S]⁺ and (b) [2Fe-4S]²⁺ after CPE.

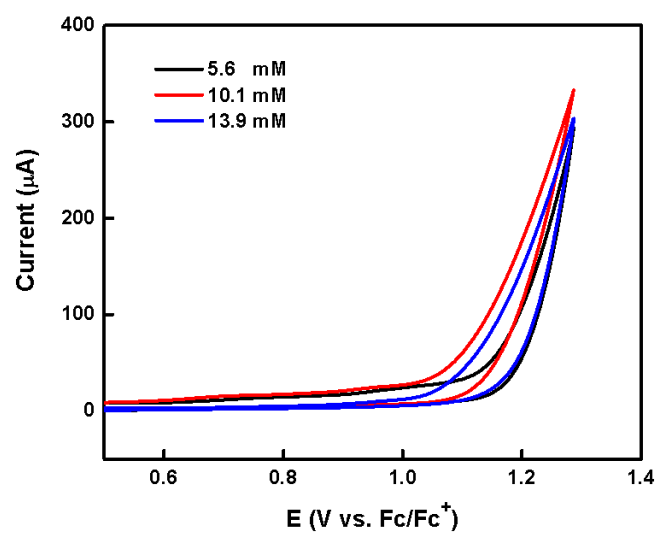


Figure S16 CVs of Fe-2S measured in MeCN/H₂O (9:1, the concentration of H₂O: 5.6 mM, black line, 8:2, the concentration of H₂O: 10.1 mM, red line, 7:3, the concentration of H₂O: 13.9 mM, blue line), respectively.

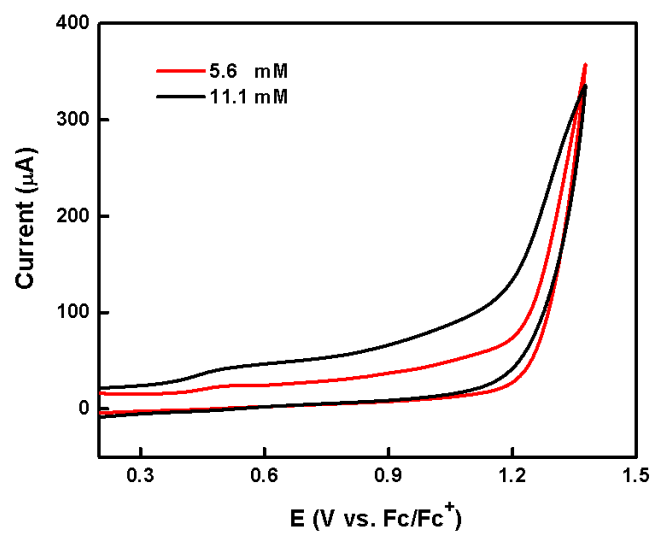


Figure S17 CVs of 2Fe-4S measured in MeCN/H₂O (9:1, the concentration of H₂O: 5.6 mM, red line) and MeCN/H₂O (8:2, the concentration of H₂O: 11.1 mM, black line), respectively.

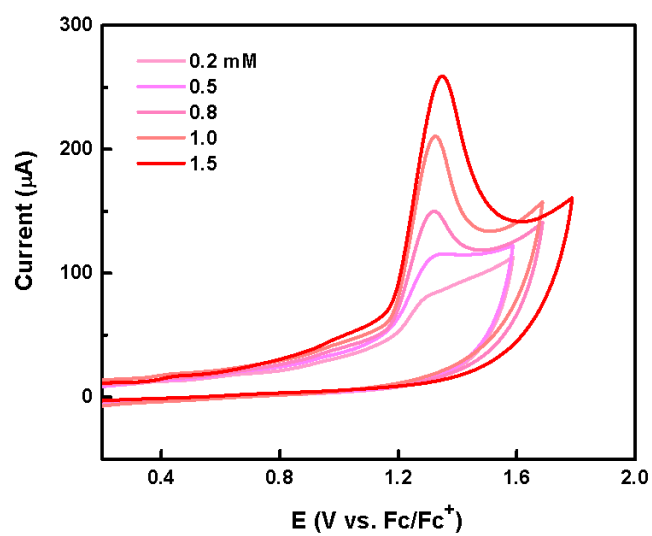


Figure S18 CVs of Fe-2S at various concentrations in MeCN.

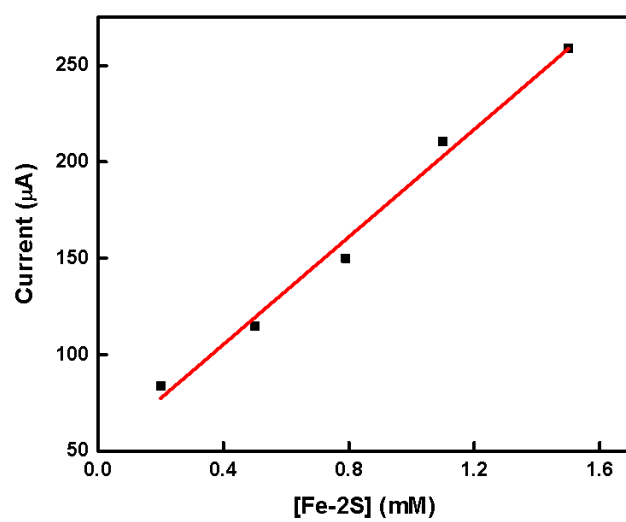


Figure S19 The relationship of peak current with Fe-2S concentration ([cat]).

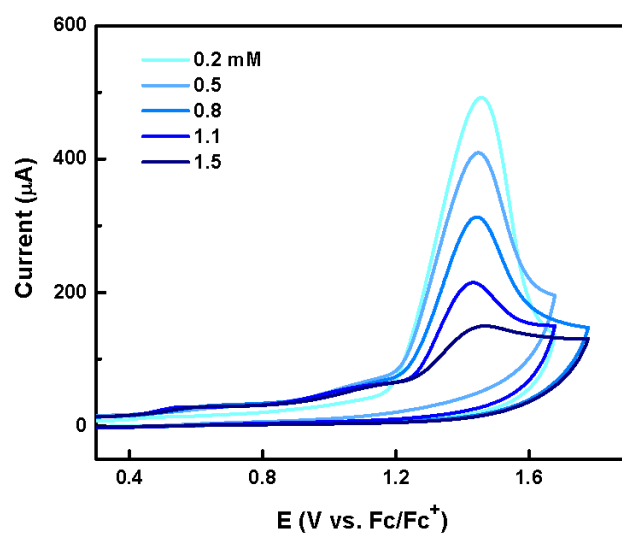


Figure S20 CVs of 2Fe-4S at various concentrations in MeCN.

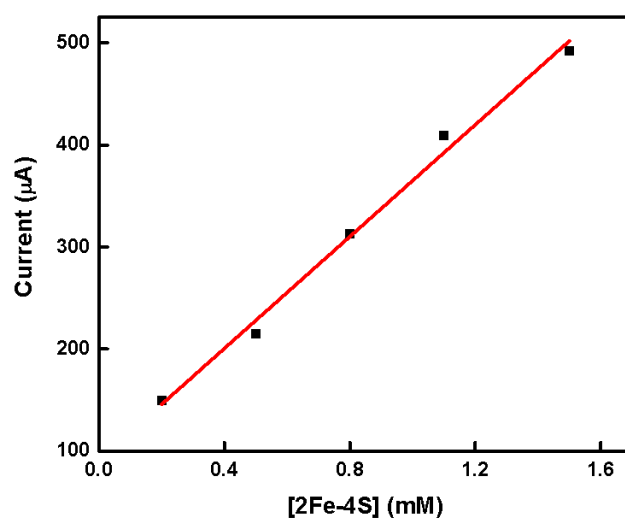


Figure S21 The relationship of peak current with 2Fe-4S concentration ([cat]).

TOF Calculation from Cyclic Voltammetric Measurements

When the current is limited only by catalytic steps in solution, under purely kinetic conditions, CVs are predicted to be S-shaped and reach a limiting catalytic current, i_{cat} , which can be expressed by the following equation (Eq. S1) and is independent of the scan rate.

$$i_{cat} = n_{cat}FA[cat]_0\sqrt{D(k[S])} \quad \text{Eq. S1}$$

where n_{cat} is the number of electrons transferred during the catalytic event, F is the Faraday's constant, A is the surface area of electrode [cm^2], $[cat]_0$ is the concentration of the catalyst, $[S]$ is the concentration of the substrate, k is the second-order rate constant and D [$\text{cm}^2\cdot\text{s}^{-1}$] is the diffusion coefficient of the catalyst.

Assume that the concentration of substrate does not change significantly during the measurement, the catalytic turnover frequency (TOF) can be expressed as a pseudo first-order rate constant, k_{cat} ($k_{cat} = k[S] = \text{TOF}$). Therefore i_{cat} can be expressed as follows.

$$i_{cat} = n_{cat}FA[cat]_0\sqrt{k_{cat}D} \quad \text{Eq. S2}$$

On the other hand, the peak current for reversible electrochemical couples, i_p , is governed by Randles-Sevcik equation (Eq. S3) as follows,

$$i_p = 0.4463n_pFA[cat]_0\sqrt{\frac{n_pFDv}{RT}} \quad \text{Eq. S3}$$

where n_p is the number of electrons transferred associated with reversible electrochemical couples, R is the universal gas constant, T is the temperature, and v is the scan rate. The ratio of i_{cat} (Eq. S2) to i_p (Eq. S3) is given by Eq. S4.

$$\frac{i_{cat}}{i_p} = \frac{n_{cat}}{0.4463n_p} \sqrt{\frac{k_{cat}RT}{n_pFv}} \quad \text{Eq. S4}$$

In the present study, i_p values were estimated from the one-electron redox process of $\text{Fe}^{\text{III}}_2/\text{Fe}^{\text{II}}\text{Fe}^{\text{III}}$ and four electrons were assumed to pass for each O_2 molecule produced. Therefore, n_p and n_{cat} values were determined to be 2 and 4, respectively.

Considering the faradaic efficiency of the reaction is 98.6% and 95.2%, the turnover frequency (k_{cat}) can be calculated from the slope of a plot of i_{cat}/i_p against $v^{-1/2}$, C , using equation Eq. S5.

$$k_{cat} = 6.7 \times 10^{-2} \frac{FC^2}{RT} \quad \text{Eq. S5}$$

The requirements to obtain TOF values using Eq. S5 are as follows:

- (1) The rate constant of the reaction should be first-order to the concentration of the catalyst.
- (2) i_p and $v^{1/2}$ should have a linear relationship to follow the Randles-Sevcik equation.
- (3) i_{cat} should be independent to scan rates to obtain a purely kinetic condition.
- (4) The amount of the substrate should be large enough to obtain a TOF (k_{cat}) value as a pseudo first-order rate constant.

The condition to satisfy these requirements for our catalyst was determined by several electrochemical measurements shown below.

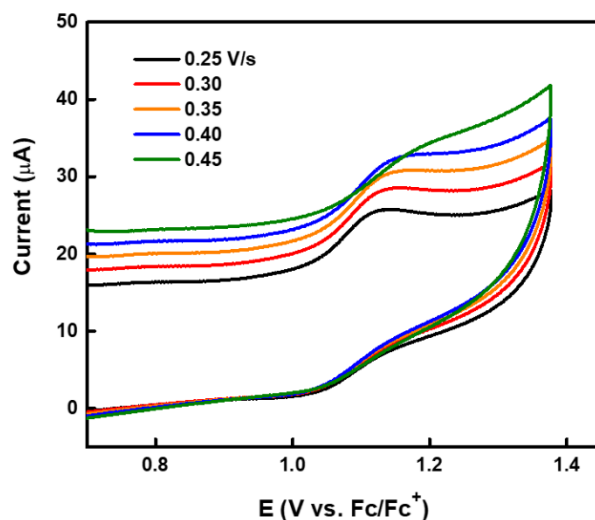


Figure S22 CVs of **2Fe-4S** in the absence of water at various scan rates.

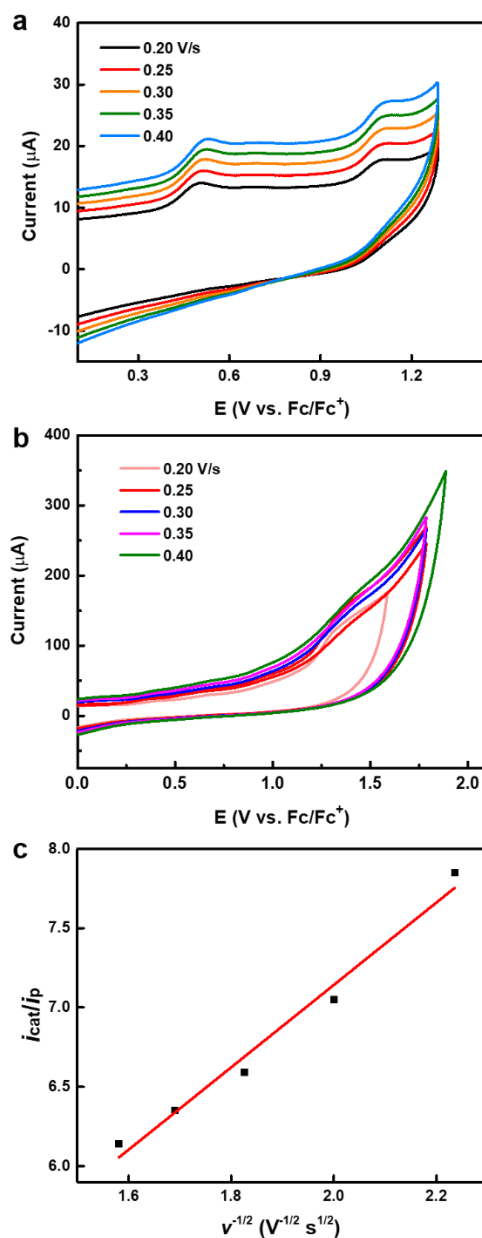


Figure S23 (a) Cyclic voltammograms of Fe-2S (0.2 mM) in the absence of water at various scan rates. (b) CVs of Fe-2S (0.2 mM) in a MeCN/ H_2O (8:2) with 0.1 M Bu_4NPF_6 , scan rates 0.2–0.4 V s^{-1} . (c) Plot of i_{cat} to i_{p} ratio versus $v^{-1/2}$ for Fe-2S.

Table S7 Summary of the numerical data in the electrochemical measurements for **Fe-2S**. Plots of i_p vs. $V^{1/2}$, i_{cat} vs. v , and i_{cat}/i_p vs. $v^{-1/2}$ are shown in Figure 3.

v (V s ⁻¹)	$v^{1/2}$ (V ^{1/2} s ^{-1/2})	$v^{-1/2}$ (V ^{-1/2} s ^{1/2})	i_{cat} (μA)	i_p (μA)	i_{cat}/i_p
0.20	0.447	2.236	140.2	17.87	7.85
0.25	0.500	2.000	144.4	20.47	7.05
0.30	0.548	1.826	150.9	22.91	6.59
0.35	0.592	1.690	158.5	24.97	6.35
0.40	0.632	1.581	167.4	27.22	6.14

Table S8 Summary of the numerical data in the electrochemical measurements for **2Fe-4S**. Plots of i_p vs. $V^{1/2}$, i_{cat} vs. v , and i_{cat}/i_p vs. $v^{-1/2}$ are shown in Supplementary Figure 3.

v (V s ⁻¹)	$v^{1/2}$ (V ^{1/2} s ^{-1/2})	$v^{-1/2}$ (V ^{-1/2} s ^{1/2})	i_{cat} (μA)	i_p (μA)	i_{cat}/i_p
0.25	0.500	2.000	355.7	25.02	14.22
0.30	0.548	1.826	374.8	28.22	13.28
0.35	0.592	1.690	377.1	30.86	12.22
0.40	0.632	1.581	390.4	33.21	11.76
0.45	0.671	1.491	383.3	35.94	10.66

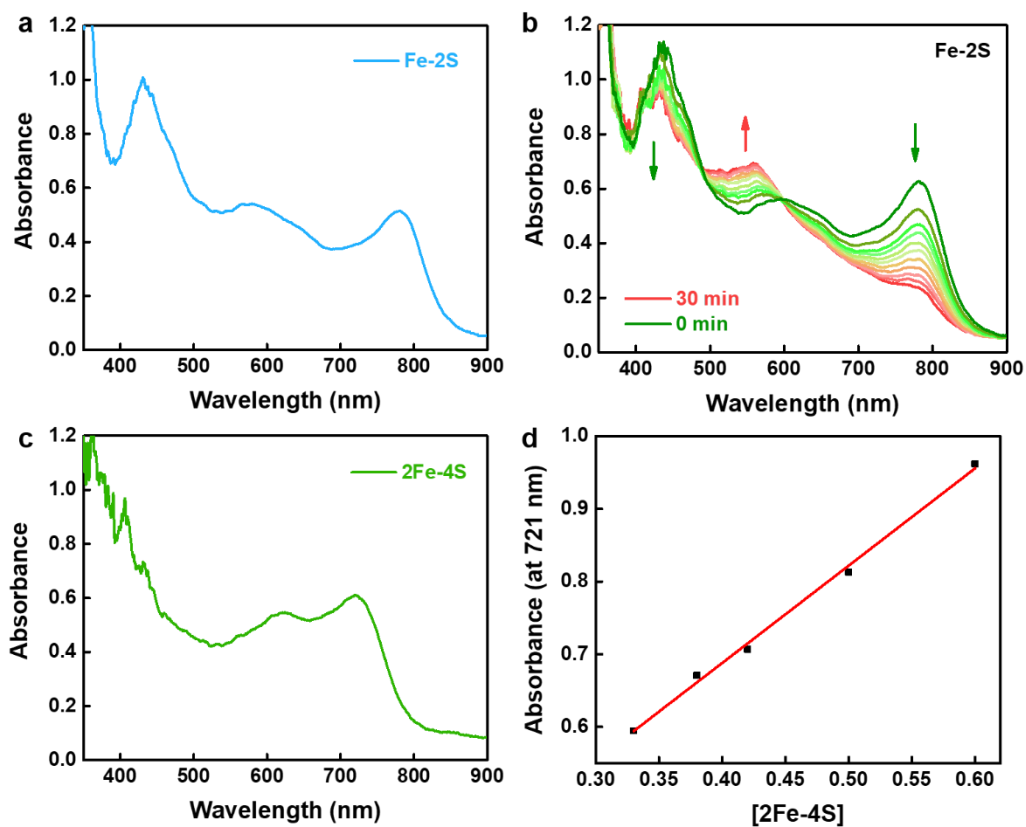


Figure S24 UV-Vis spectra of (a) **Fe-2S** and (b) change during water oxidation for **Fe-2S**. UV-Vis of (c) **2Fe-4S**. Correlation between **2Fe-4S** concentration and absorbance at 721 nm.

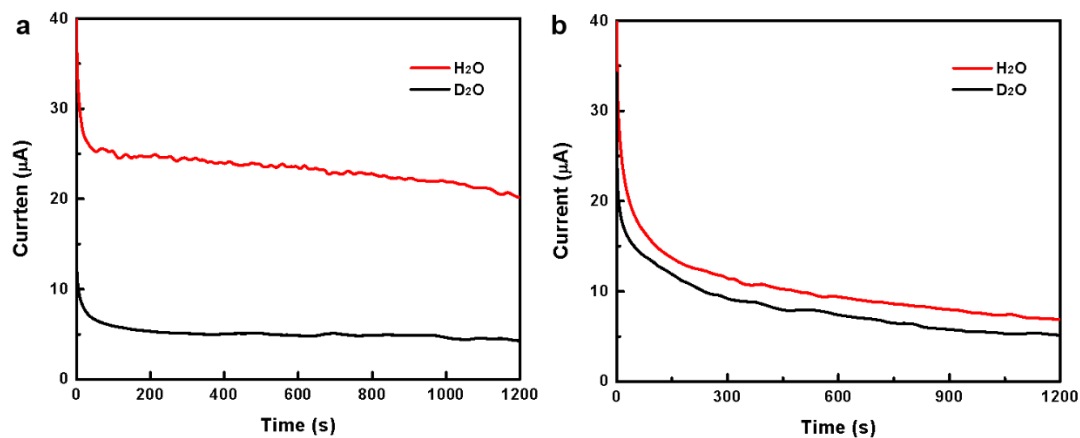


Figure S25 I-t curves of (a) **Fe-2S** and (b) **2Fe-4S** conducted at the bias of each half-wave potential in pH=7.0 and pD=7.0 solutions.

Reference

1. N. F. Chilton, R. P. Anderson, L. D. Turner, A. Soncini and K. S. Murray, *J. Comput. Chem.*, 2013, **34**, 1164—1175.